Int J Thermophys (2010) 31:1092–1110
DOI 10.1007/s10765-010-0822-9

Experimental and Theoretical Characterization of Emission from Ceramics at High Temperature: Investigation on Yttria-Stabilized Zirconia and Alumina

A. Delmas · L. Robin-Carillon · F. Oelhoffen · T. Lanternier

Received: 19 May 2009 / Accepted: 10 September 2010 / Published online: 25 September 2010

Abstract This study is a contribution to characterizations of non-isothermal ceramic samples, for mean temperatures higher than 1000 °C. The objective is to determine the infrared radiative emission, of materials often used as thermal barrier coatings, under realistic thermal boundary conditions. The problem is treated by both experimental and numerical approaches that reveal additional ways of investigation. Results from sintered zirconia and plasma-sprayed alumina are presented. The experimental bench, designed and built to perform emission measurements on semi-transparent ceramics at high temperature, is described. The numerical code used to solve coupled conduction–radiation heat transfers in semi-transparent media is introduced. Special attention is paid to calculation of radiative properties of plasma-sprayed samples characterized by their complex internal microstructure. Experimental and theoretical emission factors obtained from these kinds of ceramics samples are compared and analyzed. The influence of the inside temperature gradient on emission is discussed.

Keywords Ceramics · Coupled conduction–radiation model · Emission spectroscopy · High temperature · Radiative heat transfer · Scattering

List of symbols

E Electric field, $\mathrm{V \cdot m^{-1}}$
F_λ Spectral emission factor
h Mean convective coefficient, $\mathrm{W \cdot m^{-2} \cdot K^{-1}}$

A. Delmas (✉)
INSA-Lyon, CETHIL, UMR5008, 69621 Villeurbanne, France
e-mail: agnes.delmas@insa-lyon.fr

L. Robin-Carillon · F. Oelhoffen · T. Lanternier
CEA, DAM, CESTA, 33114 Le Barp, France

H	Magnetic field, T
I_λ	Spectral radiative intensity, $\mathrm{W \cdot m^{-2} \cdot sr^{-1} \cdot \mu m^{-1}}$
n, k	Optical indexes
p	Phase function
Q_{scat}	Scattering efficiency
q_{r}	Radiative heat flux, $\mathrm{W \cdot m^{-2}}$
r	Particle radius, m
T	Temperature, K
x	Spatial position
w	Width, m

Greek symbols

κ	Volume absorption coefficient, $\mathrm{m^{-1}}$
λ	Wavelength, μm
k_{c}	Thermal conductivity, $\mathrm{W \cdot m^{-1} \cdot K^{-1}}$
σ	Volume scattering coefficient, $\mathrm{m^{-1}}$

Subscripts

b	Relative to a blackbody
λ	Spectral
Ch	Christiansen
inc	Incidence
obs	Observation
scat	Scattering

1 Introduction

Over the last decade, much research has been dedicated to improvement and optimization of ceramic thermal barrier coatings (TBCs). The main identified high-temperature application domains of TBCs are gas turbines, for either increasing the inlet temperature to improve efficiency, or for reducing the requirements for the cooling system leading to an increase in the cooling performance of the turbine airfoil [1–7]. TBCs are used in jet engine applications, but also in the aerospace sector as protections on objects and vehicles entering the atmosphere.

The thickness of ceramic coatings may vary from 0.1 mm to 1 mm, according to the aimed application. TBCs are commonly submitted to high radiative and convective heat fluxes from the environment on one side; consequently, they must withstand high temperatures ($T > 1500\,^{\circ}\mathrm{C}$) without any damage under strong temperature gradients. Alumina (Al_2O_3) and zirconia (ZrO_2) have proved to offer the best possibilities for most mentioned applications.

Most studies are dedicated to mechanical problems, related to the adhesion of ceramic deposits on super alloy substrates, and the strain tolerance of the porous structure of ceramics [8]. More recently, studies on TBCs relate to the thermal behavior of ceramic coatings [9]. The dielectric oxides that constitute most ceramics used

for these applications are semi-transparent materials (STMs); radiative heat transfer inside the coating is responsible for a decrease in the thermal insulation performances of the barrier. However, many previous studies assume that TBCs are opaque materials, considering only conductive heat transfer in the ceramic layer.

Another important issue is the way the radiative emission from TBCs is taken into account in the overall heat balance of the system (coating-metal substrate-environment). The radiative emission in this configuration being strongly linked to the internal temperature field [10], the use of an emission factor (emissivity) is valid provided that the reference temperature is perfectly identified and relevant.

Previous studies were devoted either to emissivity determination of ceramic samples under isothermal conditions [11–14] or to accurate prediction of temperature distributions in ceramics [15,16]. The present research is a contribution to characterizations of non-isothermal TBCs for mean temperatures higher than $1000\,^{\circ}C$. The main objective is to determine the infrared radiative emission of ceramic samples under realistic thermal boundary conditions that correspond to samples submitted to high heat flux on one side only. We investigate alumina and yttria partially stabilized zirconia free standing samples (YPSZ). The problem is treated by both experimental and numerical approaches that reveal additional ways of investigation. An experimental bench is designed and built to perform emission measurements on ceramics at high temperatures, under steady states, but also for unsteady states. A numerical code to solve coupled conduction–radiation heat transfers in STMs was developed to predict both the exit intensity from the layer of ceramic coating, and the inside temperature distribution. The concept of emission factor for non-isothermal STMs is defined in a first step. Through a brief description of the experimental setup, flux and temperature measurement principles are introduced. The numerical code and the different models used for radiative property calculations are presented. Results for predicted and measured emission factors are compared and analyzed.

2 Emission Factor for Non-isothermal Semi-Transparent Materials

Selected samples are plasma-sprayed alumina. The references for both measurements and predictions are sintered samples of perfectly calibrated zirconia stabilized with 8 % of yttria (YPSZ). All samples are STMs.

They are indeed made by projecting or compacting powders of STM spherical grains. The involved elaborating processes are responsible for the resulting porous structure as illustrated by MEB pictures in Fig. 1a, b.

Despite the increasing number of applications of semi-transparent ceramics as thermal barriers, radiative emission spectra found in the literature for such materials still present a very large discrepancy, due to differences in material characteristics such as porosity, grain size, purity, surface roughness, and the potential inside temperature gradient. Therefore, we must consider the concept of the emission factor for STMs which is a volume property, instead of emissivity considered as a surface property for opaque materials. In a previous study, we already discussed the relevance of using this factor for temperature optical measurements [17]. The purpose is quite different here; it appears more convenient to compare the spectral emission behavior of

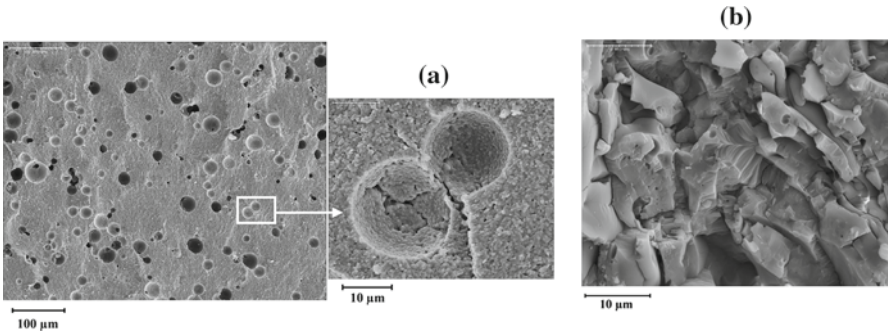

Fig. 1 (a) Sintered ZrO_2 and (b) plasma-sprayed Al_2O_3

various samples in terms of the spectral emission factor instead of the spectral intensity. Furthermore, we must highlight the fact that the emission factor is defined here for non-isothermal samples which is one of the specific points of the study.

The experimental conditions presented in the next section lead to the definition of a spectral directional emission factor for a slab heated on one side (called the forward side) with isothermal faces and an internal temperature gradient. The temperature gradient is assumed to be one-directional along the sample width; this hypothesis is justified along with the description of the experimental bench. Let us point out here that an emission factor measurement performed on a non-isothermal sample is valid, provided that the internal temperature field is jointly determined. Moreover, an emission factor must be defined for each side of the sample. Thus, the spectral directional emission factor for the forward side is defined as follows:

$$F_{\lambda,\text{forward}} = \frac{I_{\lambda,\text{forward}}}{I_{\lambda,\text{b}}[T_{\text{forward}}]} \tag{1}$$

where $I_{\lambda,\text{forward}}$ is the measured radiative spectral intensity leaving the forward face, and $I_{\lambda,\text{b}}$ is the Planck function for the measured surface temperature T_{forward} of the forward face. Although the experimental bench allows directional measurements, we present here only normal spectral emission factors.

3 Laboratory Experimental Setup and Measurement Principles

3.1 Emission Spectroscopy Bench and Measured Emission Spectra

The experimental setup has been designed to perform emitted radiative heat flux and surface temperature measurements, on both sides of the sample, under steady and unsteady states for the temperature field. Characterization of emission under a temperature gradient, and unsteady-state measurements, are the main originality of the experimental setup. The bench presented in Fig. 2 is composed of the radiative heating system, the optical assembly for forwarding emitted radiation from the sample toward

Fig. 2 High-temperature emission experimental bench

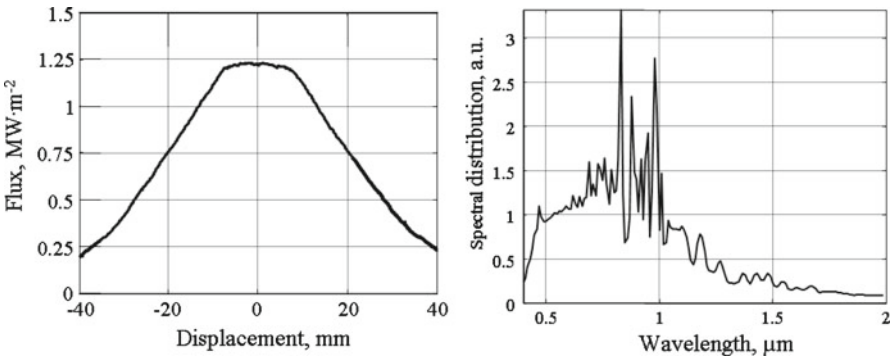

Fig. 3 Spectral and spatial distribution of the incident heat flux on the sample

the measurement device which is a Fourier transform spectrometer (FTIR). For more details, the reader may refer to [17,18].

Samples are small disks of 30 mm in diameter and are all 1 mm thick; they are irradiated on one face only, called the forward side. The heating source (Fig. 2) is an arc lamp furnace composed of four xenon arc lamps with a unitary electrical power of 7000 W. Spectral distribution of the intensity emitted by the four lamps is centered on 1 µm. A Pyrex filter stops radiation from the lamps beyond 2.7 µm (Fig. 3) in such a way that radiation measured by the FTIR between 2.7 µm and 15 µm comes only from the sample. According to spatial heat flux measurements performed with a Gardon fluxmeter [18] and presented in Fig. 3, the incident flux from the radiative heat source is homogeneous within 5 % to 1.25 $MW \cdot m^{-2}$ on a circular area of about 18 mm of diameter. Consequently, the sample surfaces may be considered as isothermal to within 5 % inside a 15 mm diameter disk. However, as long as the heating source is on, the internal temperature of the samples is not uniform. In a first step, only surface

temperatures of each face are measured with a Christiansen pyrometry technique; then the inside temperature profile is predicted performing calculations presented in Sect. 4.

The optical system to collect emission from the sample is composed of three identical paths, corresponding, respectively, to the two faces of the sample, and to a high temperature blackbody (SOC 200, Surface Optics Corp.) for calibration purposes. Beams leaving both sides of the ceramic sample alternatively reach the entrance of the spectrometer with a 8 Hz frequency directly linked to the electronic shutter speed. Emission spectra, corresponding to measurements of normal spectral radiative heat flux exiting the ceramic sample, are performed with a Fourier transform infrared spectrometer (Nexus 5700, Thermo Electron, France) for a wavelength range from 2.5 μm to 15 μm, and for both sides of the sample.

The FTIR calibration consists of an emission spectrum $S_{\lambda,\mathrm{b}}$ performed on a blackbody at a selected temperature T_b. In the little solid angle of heat flux measurement, which is the same for the three configurations (0.04 sr), the radiative intensity is assumed isotropic. Consequently calibration is directly performed in terms of the radiative intensity. Since extraneous fluxes may interfere with the measured emission spectrum, their corresponding spectrum—$S_{\lambda,\mathrm{extra}}$—is measured and deduced from the emission spectrum of the sample $S_{\lambda,\mathrm{sample}}$.

According to the previous remarks, the radiative intensity leaving the sample is given by

$$I_{\lambda,\mathrm{sample}} = \frac{I_{\lambda,\mathrm{b}}(T_\mathrm{b})}{\left[S_{\lambda,\mathrm{b}}(T_\mathrm{b}) - S_{\lambda,\mathrm{extra}}\right]}\left[S_{\lambda,\mathrm{sample}} - S_{\lambda,\mathrm{extra}}\right] \tag{2}$$

where $S_{\lambda,\mathrm{b}}$ stands for the blackbody spectrum and $I_{\lambda,\mathrm{b}}$ is the Planck function.

The extended uncertainty of the sample spectrum radiative intensity is calculated with an expanded factor equal to 2 so that 95 % of the results are in the uncertainty interval. Over the entire spectral range [2.7 μm to 13.5 μm], the expanded uncertainty is lower than 5 % and remains below 3 % over the range [5 μm to 11 μm].

From these measurements, emission factors are deduced via the previous formula [1], provided that the surface temperature, obtained via an optical method using the Christiansen phenomenon, has been previously determined to calculate Planck's function at the relevant temperature.

3.2 Surface-Temperature Optical Measurements

Surface temperatures are determined with a Christiansen pyrometry technique [17,19] for which the principle is as follows. The complex refractive index of a material is $\tilde{n}_\nu = n_\nu + \mathrm{i}k_\nu$; n_ν and k_ν depend on the wave frequency ν and on the material electrical properties. The normal spectral reflectivity (ρ_ν), at a specular interface between two media of respective indexes, $\tilde{n}_{1\nu}$ and $\tilde{n}_{2\nu}$, is given by

$$\rho_\nu = \left|\frac{\tilde{n}_{2,\nu} - \tilde{n}_{1,\nu}}{\tilde{n}_{2,\nu} + \tilde{n}_{1,\nu}}\right|^2 \tag{3}$$

According to a formula in [3], the optical interface between two media vanishes when $\tilde{n}_{1\nu} = \tilde{n}_{2\nu}$, a condition which is fulfilled provided that $n_{1,\nu} = n_{2,\nu}$ and $k_{1,\nu} = kn_{2,\nu}$.

Christiansen pyrometry is a specific application of the above phenomenon, one of the two media being air ($n_1 = 1$, $k_1 = 0$). For heteropolar dielectric materials, there are several frequencies (correspondingly, the wavelengths) over the electromagnetic spectrum for which the real part, n_2, of the refractive index is equal to one. But there is only one frequency we will refer to as Christiansen's frequency, for which k_2 is low enough to consider that there is no reflection at the interface. However, although k_2 is very low (lower than 10^{-2} at $\lambda = 10$ μm for zirconia), the radiative absorption is sufficiently substantial for an incident radiation to be totally absorbed by a hundred micron layer of the material. Then, at the Christiansen frequency, the material can be considered as a blackbody in terms of radiation. For common heteropolar materials, the corresponding Christiansen wavelength in air (or vacuum), λ_{Ch} is located in the mid-infrared range; e.g., $\lambda_{Ch} = 9.5$ μm for alumina (Al_2O_3) and $\lambda_{Ch} = 12.8$ μm for zirconia (ZrO_2). The exact location of this wavelength depends on the material but not on the temperature. It is linked to absorption mechanisms (lattice vibrations) occurring in the mid-infrared range [19].

The surface temperature of the ceramic sample is deduced from the radiative heat flux measured by pyrometry using Planck's function as follows:

$$T = \frac{hc}{k\lambda_{Ch} \ln\left[\frac{2hc^2}{\lambda_{Ch}^5 I_{\lambda Ch}} + 1\right]} \tag{4}$$

where $I_{\lambda Ch}$ is the sample spectral intensity measured in air at Christiansen's wavelength λ_{Ch} and c is the speed of the light in air ($c = c_o = 2.998 \times 10^8\,\mathrm{m \cdot s^{-1}}$, speed in vacuum), k is the Boltzmann constant ($k = 1.3806 \times 10^{-23}\,\mathrm{J \cdot K^{-1}}$), and h is the Planck constant ($h = 6.626 \times 10^{-34}\,\mathrm{J \cdot s}$).

4 Emission Factor Simulation

4.1 Governing Equations and Boundary Conditions

Emission factor prediction involves the calculation of intensity and temperature fields in the studied semi-transparent medium resulting from the coupled conduction–radiation heat transfers in the material. In this study, a macroscopic approach is chosen to simulate heat transfers governed by the coupling of the radiative transfer equation (RTE) and the energy equation. For a one-dimensional planar problem with an absorbing, emitting, and scattering medium, under the assumption of azimuthal symmetry, the classical gray-band formulation of the RTE for unpolarized radiation is given by

$$\mu \frac{\mathrm{d}I_{\Delta\nu}(x,\mu)}{\mathrm{d}x} = -(\sigma_{\Delta\nu} + \kappa_{\Delta\nu}) I_{\Delta\nu}(x,\mu) + n_{\Delta\nu}^2 \kappa_{\Delta\nu} I_{\mathrm{BB},\Delta\nu}[T(x)] + \frac{\sigma_{\Delta\nu}}{2} \int_{-1}^{1} p_{\Delta\nu}(\mu,\mu') I_{\Delta\nu}(x,\mu')\mathrm{d}\mu' \tag{5}$$

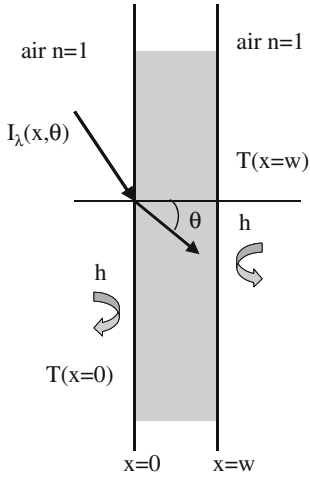

Fig. 4 Scheme of the studied configuration

where $\mu = \cos(\theta)$ (see Fig. 4); $\kappa_{\Delta\nu}$, $\sigma_{\Delta\nu}$, and $n_{\Delta\nu}$ are, respectively, the absorption coefficient, scattering coefficient, and refractive index averaged over the frequency interval $\Delta\nu$. For the forward side, radiation at the interface is a balance between losses from the emission of the sample and incoming radiation from the lamp. For the backward side, only radiative heat losses by emission are considered. Reflectivity at interfaces is calculated using Snell's law and Fresnel's equations [10] as follows:

$$I_{\Delta\nu}(x=0,\mu>0) = (1-\rho_{\Delta\nu}(\mu))I_{\Delta\nu,\mathrm{inc}} + \rho_{\Delta\nu}(\mu)I_{\Delta\nu}(x=0,\mu<0)$$
$$I_{\Delta\nu}(x=w,\mu<0) = \rho_{\Delta\nu}(\mu)I_{\Delta\nu}(x=w,\mu>0)$$

The radiative transfer equation is solved using a discrete ordinates method. An iterative process is used to include scattering and the interface reflexion phenomena [18].

In a one-dimensional planar system, the energy equation for coupled conduction/radiation heat transfer for steady state is

$$\frac{\mathrm{d}}{\mathrm{d}x}\left\{ k\,\frac{\mathrm{d}}{\mathrm{d}x}\left[T(x)\right]\right\} + \mathrm{div}(\vec{q}_\mathrm{r}) = 0 \tag{6}$$

The associated boundary conditions at $x = 0$ and $x = w$ are

$$\begin{cases} k_\mathrm{c}\dfrac{\mathrm{d}T}{\mathrm{d}x}\Big|_{x=0} = h(T_{x=0} - T_\mathrm{sur}) \\ k_\mathrm{c}\dfrac{\mathrm{d}T}{\mathrm{d}x}\Big|_{x=w} = -h(T_{x=w} - T_\mathrm{sur}) \end{cases} \tag{7}$$

The source term of the energy equation is calculated as follows:

$$\operatorname{div}(\vec{q}_{\mathrm{r}}) = 2\pi \int_0^{\infty} \frac{\mathrm{d}}{\mathrm{d}x} \left[\int_{-1}^{1} \mu I_{\Delta\nu}(x) \mathrm{d}\mu \right] \mathrm{d}\nu \tag{8}$$

From simulated intensity and temperature fields in the ceramic slab, emission factors are calculated as given by Eq. 1 for forward and backward sides, respectively:

$$F_{\lambda}(T[0],0) = \frac{I_{\lambda}(\mathrm{x}=0)}{I_{\lambda,\mathrm{b}}(T[\mathrm{x}=0])}; \quad F_{\lambda}(T[\mathrm{w}],\mathrm{w}) = \frac{I_{\lambda}(\mathrm{x}=\mathrm{w})}{I_{\lambda,\mathrm{b}}(T[\mathrm{x}=\mathrm{w}])} \tag{9}$$

4.2 Thermal Conductivity and Radiative Properties

Input data for simulations are thermal conductivity and radiative properties of materials for the studied samples that have a porosity rate of 20 % for the sintered samples and of 9 % for the plasma-sprayed ones.

The thermal conductivity depends on the temperature and sample microstructure. Furthermore, for stabilized zirconia samples, the thermal conductivity also depends on the fraction of yttria (8 %). The thermal conductivity of alumina and yttria-stabilized zirconia are, respectively, given by Clarke [20] (8 $\mathrm{W \cdot m^{-1} \cdot K^{-1}}$ at 1273 K) and McPherson [21] (1.3 $\mathrm{W \cdot m^{-1} \cdot K^{-1}}$). The value of the convective heat transfer coefficient used for the present simulations is equal to 10 $\mathrm{W \cdot m^{-2} \cdot K^{-1}}$ and assumed to be representative of the case of a vertical slab in air. Absorption and scattering spectral volumetric coefficients, as well as phase functions, are calculated from optical indexes and microstructure parameters of the materials. For the sintered and plasma-sprayed structures, materials are assumed to be composed of an absorbent matrix (ceramic), homogeneous in terms of optical indexes, containing air-filled pores that are the scattering particles. Scattering by grain boundaries is neglected. Furthermore, the porosity rate and particle size lead to a sufficiently large clearance between two particles relative to both the radiation wavelength (0.3 μm to 15 μm) and the particle diameter, to assumed independent scattering [10].

Because of the low porosity rate of the studied samples ($\leq$20 %), refractive indexes are assumed to be equal to that of the relevant monocrystal of the dielectric oxide. These indexes depend on frequency (correspondingly the wavelength) and temperature. They have been measured by the CEMHTI laboratory as a function of wavelength in the range [0.4 μm to 25 μm] at 1300 K for yttria-stabilized zirconia and at 1170 K for alumina. The spectral volumetric absorption coefficient is evaluated from the imaginary part of the measured refractive index of the bulk ceramic as follows:

$$\kappa_{\lambda} = \frac{4\pi k_{\lambda}}{\lambda}$$

Scattering coefficients and phase functions are not evaluated by the same method for sintered samples and plasma-sprayed ones because of fundamental differences in their respective microstructures.

The scattering coefficient and the phase function for YPSZ-sintered samples are calculated by the classical Mie theory. Samples are obtained by sintering zirconia

powder with the addition of a pore-forming material. Consequently, pores are spherical and their radius distribution $d(r)$ is perfectly known and centered on 10 μm [18]. σ_i and p_i are, respectively, the scattering coefficient and the phase function for particles of each radius calculated by the Mie theory. Global properties of a sample are obtained by integrating single previous properties as follows:

$$\sigma = \int_0^\infty \sigma_i(r) d(r)\, \mathrm{d}r \tag{10}$$

$$p(\mu, \mu') = \frac{1}{\sigma} \int_0^\infty \sigma_i(r)\, p_i(r, \mu, \mu') d(r)\, \mathrm{d}r \tag{11}$$

The well-characterized microstructure, and the classical theory used to determine radiative properties, make them reference samples for our study. The spectral volumetric scattering coefficient σ_λ determined with this approach, and the spectral volumetric absorption coefficient κ_λ calculated from [9] are presented in Fig. 5.

The approach used to calculate the radiative properties of plasma-sprayed samples is more complex than the one relative to sintered ones, because of the chaotic microstructure of the material. According to Ilavsky [22], three main void systems can generally be identified in plasma-sprayed materials as illustrated in Fig. 6—(a) globular spherical pores, (b) interlamellar pores of ellipsoidal geometry mostly parallel to the sample surface, and (c) intralamellar pores of ellipsoidal geometry which are perpendicular to the sample surface.

For the prediction of radiative properties, only types a and b are considered. Intralamellar cracks indeed disappear while the sample temperature increases during heating, because of strain relaxation [23]. Under the assumption of independent scattering,

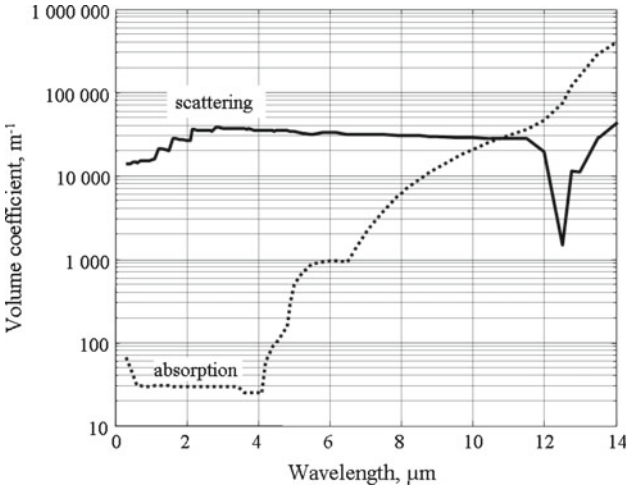

Fig. 5 Absorption and scattering spectral coefficients for YPSZ

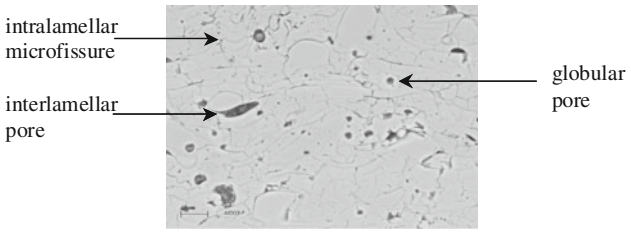

Fig. 6 Representative microstructure of plasma-sprayed materials

global scattering properties of the material are calculated from the scattering coefficient and phase function corresponding to each particle as a function of their volume fraction [10]. Radiative properties of globular pores are calculated by the Mie theory. For interlamellar pores, an electromagnetic approach is chosen to take into account their ellipsoidal shape and its preferential orientation. The electromagnetic fields resulting from the interaction between a plane wave and a particle are calculated by means of a three-dimensional (3-D) electromagnetic code (Heliot [24]).

Radiative properties (scattering efficiency Q_{scat} and phase function $p(\theta_{\text{inc}}, \theta_{\text{obs}})$) are then given by the following expression:

$$Q_{\text{scat}} = \frac{W_{\text{scat}}}{W_{\text{inc}}} \tag{12}$$

$$W_{\text{scat}} = \frac{1}{2} \int_{S_{\text{particle}}} \Re \left\{ \vec{E}_{\text{scat}} \wedge \vec{H}^*_{\text{scat}} \right\} \vec{n} \, \mathrm{d}s \tag{13}$$

$$W_{\text{inc}} = \frac{1}{2} \int_{\frac{1}{2} S_{\text{particle}}} \Re \left\{ \vec{E}_{\text{inc}} \wedge \vec{H}^*_{\text{inc}} \right\} \vec{n} \, \mathrm{d}s \tag{14}$$

$$p(\theta_{\text{inc}}, \theta_{\text{obs}}) = \frac{\Re \left\{ \vec{E}_{\text{scat}} \wedge \vec{H}^*_{\text{scat}} \right\} \vec{n}}{W_{\text{inc}}} \tag{15}$$

An important point is that the volumetric scattering coefficient of ellipsoids depends only on the incident angle (θ_{inc}), while the phase function depends on both the incident (θ_{inc}) and observation (θ_{obs}) angles as represented in Fig. 7.

Fig. 7 Scheme of the ellipsoid to model included pores

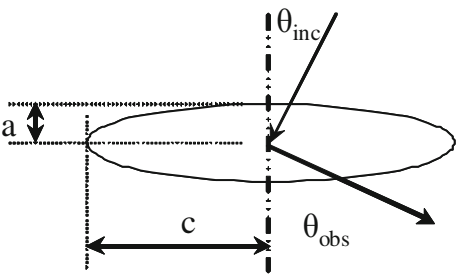

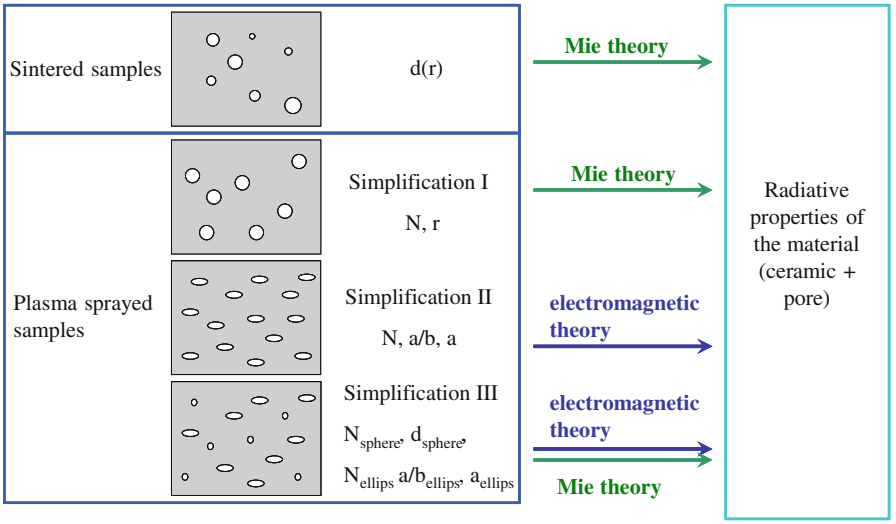

Fig. 8 Principle of radiative property calculations

To model the chaotic complex microstructure of plasma-sprayed materials, simplifying assumptions are required. Moreover, the microstructure parameters of these materials are not easy to measure and those available depend on the characterization technique, which is either mercury intusion porosimetry or MEB image analysis. Three steps of simplifying assumption were used throughout this study. They are detailed below and referred to as simulations I, II, and III.

For *Simulation I*, the sample is assumed to be composed of a ceramic matrix with *spherical* inclusions; essential parameters are the number of particles N per unit volume and the mean diameter d of these particles that are both provided by mercury intrusion porosimetry. In *Simulation II*, the ceramic matrix includes *ellipsoidal* particles; N and the mean parameters, a, $b = a$, and c, of ellipsoids are given by MEB analysis. *Simulation III* corresponds to a ceramic matrix with *ellipsoidal and spherical* inclusions; the number of spheres and the number of ellipsoids per unit volume, respectively, N_{sphere} and N_{ellips}, as well as the mean specific parameters, sphere radius r and a, $b = a$, and c, for ellipsoids, come from MEB analysis.

Depending on the particle shape, scattering properties are determined either by the Mie theory for spheres, or through an electromagnetic approach for ellipsoids, as illustrated in Fig. 8.

For alumina plasma-sprayed samples, parameters used for the three simulations are given in Table 1.

5 Results and Discussion for Predicted and Measured Emission Factors

5.1 Reference Sample: Sintered Zirconia (ZrO_2)

These preliminary tests consist of comparing the simulated and measured emission factors of sintered yttria-stabilized zirconia, for isothermal samples. The selected

Table 1 Microstructure parameters for alumina plasma-sprayed samples

	Geometrical form	Volume fraction (%)	Geometrical parameters
Simulation I	Spheres	9	$r = 100$ nm
Simulation II	Ellipsoids	9	0.75 μm, 0.75 μm, 0.3 μm
Simulation III	Spheres	0.63	$r = 200$ nm
	Ellipsoids 1	5.22	0.7 μm, 0.7 μm, 0.07 μm
	Ellipsoids 2	3.15	0.75 μm, 0.75 μm, 1 μm

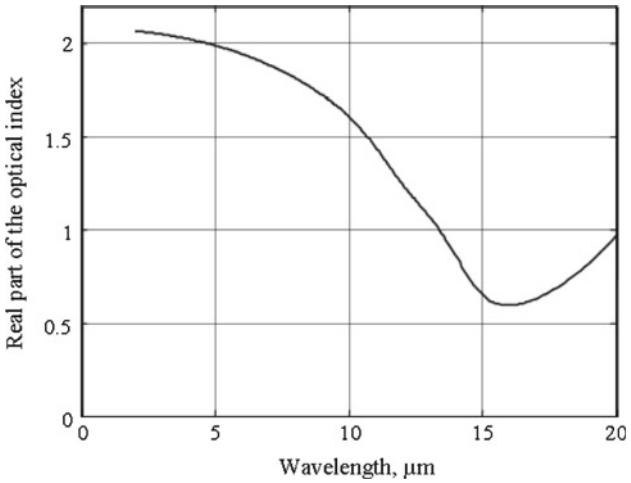

Fig. 9 Real part of the optical index of YPSZ

temperature value for simulations and measurements is 1300 K; it is imposed by the temperature at which the optical indexes are available and measured by CEMHTI (Figs. 9, 10).

For our experiments, this temperature can only be reached during the cooling phase because the power control of the arc lamp furnace does not allow obtaining this specific temperature under steady state. Moreover, during the cooling phase, the axial temperature gradient in the sample is very low (<30 K $\cdot$ mm^{-1}), allowing comparison between the isothermal simulated emission factor with the experimental one. As mentioned previously, indexes are measured on the monocrystal of the corresponding dielectric oxide, which is for this case zirconia stabilized with 8 % in mass of yttria. In Fig. 11, calculated and measured emission factors in the previous conditions are presented for comparison purposes, showing very good agreement between the two factors.

This type of sample, selected for their well-characterized microstructure, can really be considered as a reference for this study. The encouraging results on the comparison of emission factors suggest good confidence in both the measurement principle and the macroscopic theoretical approach used to simulate the emission factor. A small discrepancy is however observed in the spectral range [2.7 μm to 4.5 μm]. For short

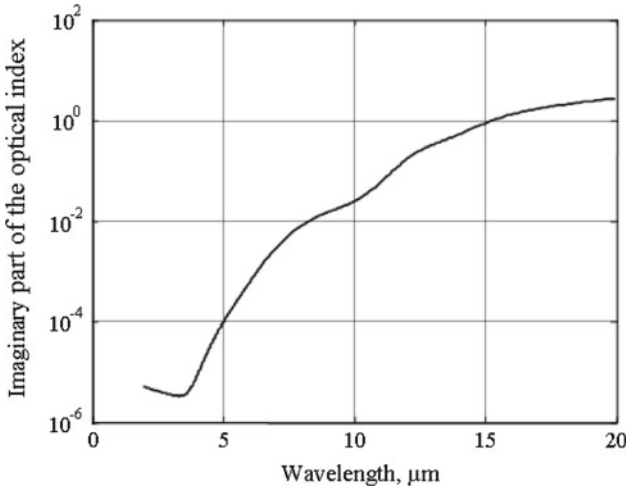

Fig. 10 Imaginary part of the optical index of YPSZ

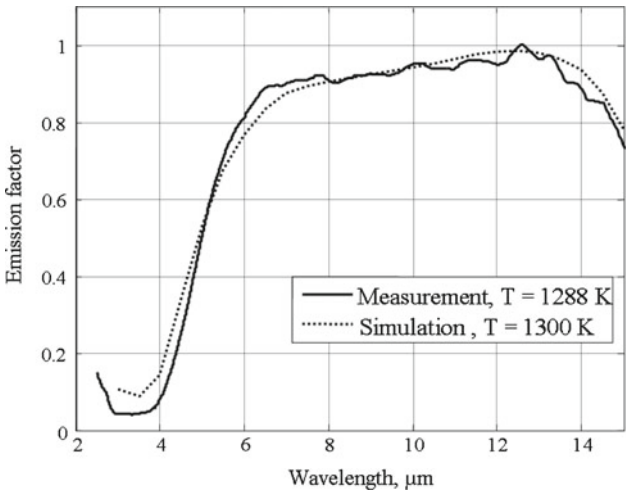

Fig. 11 Predicted and measured emission factors of sintered YPSZ

wavelenghts, the imaginary part of the optical index of YPSZ is lower than 10^{-5} (Fig. 10); this leads to a large uncertainty in measurements that affects the calculation of the absorption coefficient (Eq. 9) and consequently the predicted emission factor in this wavelength range.

5.2 Plasma-Sprayed Alumina (Al_2O_3)

For plasma-sprayed alumina material, the experimental emission factor has been measured at steady state, under a resulting temperature gradient lower than 30 K · mm^{-1}.

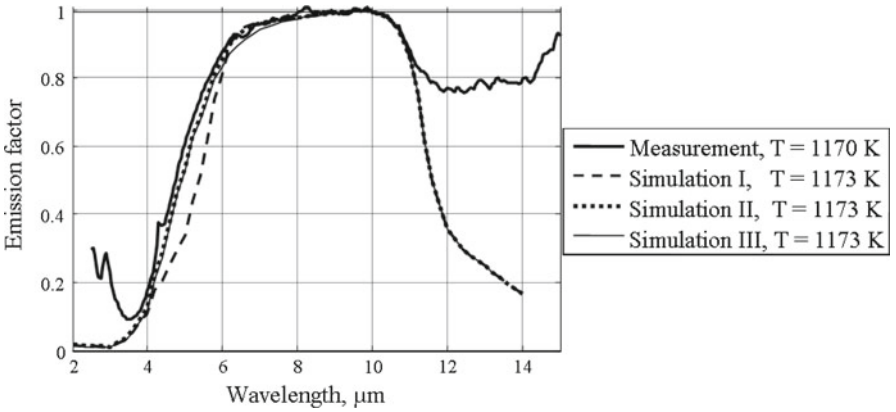

Fig. 12 Predicted and measured emission factors of plasma-sprayed Al_2O_3

The theoretical emission factor is predicted for an isothermal configuration at 1173 K, and for the three microstructure simulations detailed in Sect. 4.2 (See Fig. 12).

In Fig. 12, good agreement is observed between the experimental and the theoretical emission factors for *Simulations II* and *III*, and in the following spectral range [2 μm to 11 μm]. Above 11 μm, the discrepancy between simulations and measurement may be explained by the fact that the sample surface roughness has not been taken into account in the simulations. In this wavelength range, the volume scattering is indeed low when compared to absorption, and radiation is only scattered at the surface of the sample. The emission factor is significantly reinforced by this surface scattering, a phenomenon that is not taken into account in simulations, but can be observed on the experimental curve. We can confirm that additional information is provided by experimental and numerical approaches performed simultaneously. The comparison also suggests the necessity of modeling the real surface roughness.

In *Simulation I*, the material is assumed to be made of a ceramic matrix with spherical inclusions whose radius is provided by mercury porosimetry ($r = 100$ nm). This characterization technique proved awkward for sprayed deposits [22]; because of the complex void system of that type of material, the use of mercury intrusion porosimetry leads to a mean diameter of pores that is not representative of the characteristic particle dimension. The direct consequence is an underestimation of the emission factor in the spectral range, 4 μm to 6 μm.

For the spectral range below 4 μm, the measured emission factor is higher than the simulated ones and a peak is observed around 3 μm. The presence of hydroxyl groups in the ceramic material used for our experiments may be responsible for this discrepancy. In fact, optical indexes used for simulations are those of the corresponding monocrystalline samples in which there are no hydroxyl groups.

Simulations II and *III* lead to similar predicted emission factors over the whole studied spectral range.

The relevant parameters that seem to significantly influence the emission factor are the total porosity rate and the scattering particle size more than the particle shape. Furthermore, the thickness of the sample is also a parameter of influence on the emis-

sion factor of semi-transparent materials all the more as the material is optically thin in the considered spectral range.

5.3 About the Relevancy of Using an Emission Factor

A final objective of this study is to define the validity and the operational limits of using an emission factor, for non-isothermal semi-transparent materials, the choice of a reference temperature being the key parameter. Measured spectra on various ceramics commonly used as TBCs confirm that the definition of an emission factor under a temperature gradient requires many cautions, and cannot be considered as an intrinsic property of a material. Indeed, emission measurements performed on one hand during the heating phase when the sample is non-isothermal, and on the other hand during the cooling phase when the material is almost isothermal, showed different values of the emission factor for the same measured surface temperature (on the front or back face). This phenomenon is illustrated in Fig. 13. On this graph, values of measured emission factors for a YPSZ reference sample are plotted versus surface temperature measured on the relevant face of the sample by Christiansen pyrometry. These data correspond either to the front face, or to the back face, for measurements performed during heating or cooling.

For short wavelengths, illustrated here by measurements at 4 μm, optical properties of YPSZ are strongly dependent on the temperature [25]. A significant increase in the emission factor is observed with an increase of the surface temperature, a phenomenon observed on front and back sides of the sample. During the heating, the emission factor measured on the back face at 1500 K is twice the value measured at 1000 K; from 1000 K to 1800 K the emission factor is multiplied by 10. This phenomenon is not

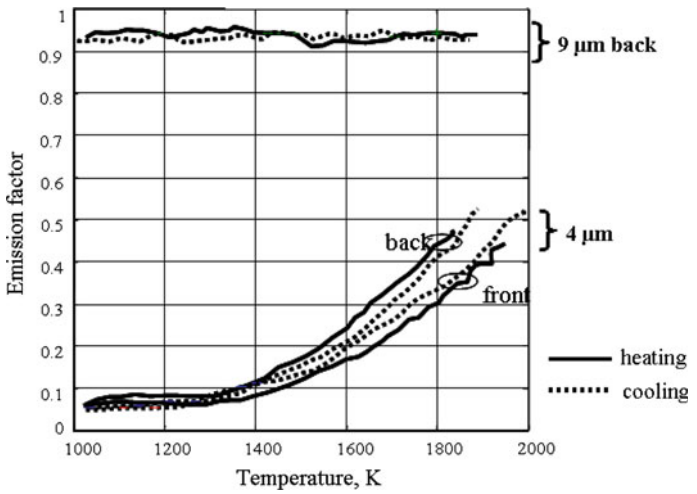

Fig. 13 Influence of the temperature gradient on the measured emission factors of sintered-YPSZ during heating and cooling phases

observable in the mid-infrared range; as shown in Fig. 13, measurements performed at 9 μm on both sides are independent of temperature.

Moreover, the influence of the inside temperature gradient (Fig. 14) on the spectral emission factor, can be observed in the near-infrared range illustrated here at 4 μm; the noticeable difference in the emission factor between the back and the front faces for the same surface temperature during heating is a direct consequence of the inside temperature gradient. During heating, for $T_{\text{forward}} > 1400$ K, the value of the temperature difference between the two faces divided by the sample thickness is higher than 70 K · mm^{-1} (Fig. 15).

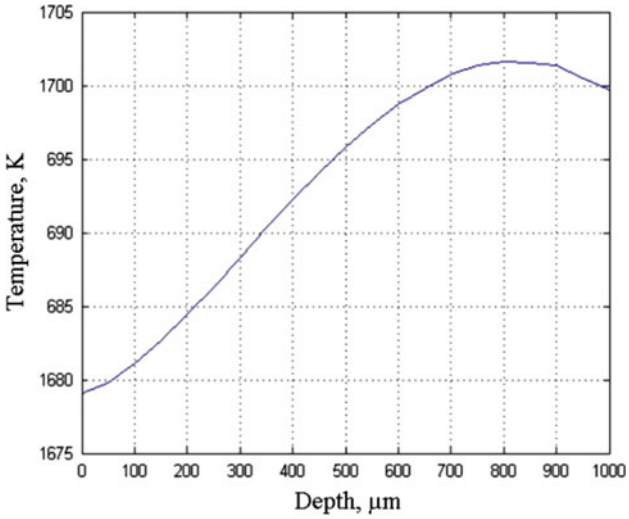

Fig. 14 Calculated temperature profile inside a YPSZ-sintered sample during heating

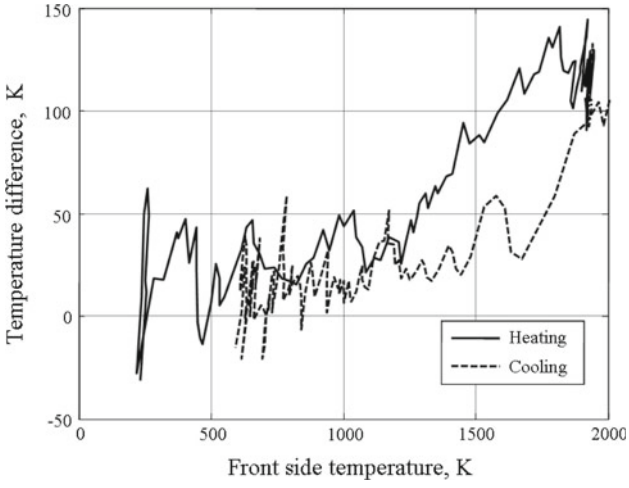

Fig. 15 Temperature difference measured on a YPSZ-sintered sample during heating and cooling phases

One can also notice that the back emission factor is higher than the front one because of volume emission in a non-isothermal material. When cooling the sample, as soon as the heating lamps are shut off, the temperature decreases drastically; in a few seconds the temperature difference between the front and the back faces is lower than 50 K (see Fig. 14). For $T_{\text{forward}} < 1500$ K, the sample can be assumed isothermal and there is no difference between the front and the back emission factors for the same surface temperature (see Fig. 13). In the mid-infrared the sample is optically thick, and as expected, there is no difference between the front and the back emission factors as suggested by measurements at 9 μm presented in Fig. 13.

6 Conclusions

An experimental bench design to measure emission spectra from ceramics used as TBCs has been carried out. The innovative part of this setup lies in the possibilities of measurements on non-isothermal materials, under steady and unsteady states. In this study are presented measurements performed on YPSZ and Al_2O_3, which are standard materials for TBCs, in the normal direction from samples surfaces.

At the same time, a one-dimensional numerical code that solves coupled conduction–radiation heat transfers in semi-transparent media is developed, based on the governing energy and radiative transfer equations. For radiative property calculations, both materials are considered made of pores, constituting the scattering particles embedded in an absorbing matrix. Sintered YPSZ samples, presenting well-controlled and characterized spherical pores, are considered as references for experimental and numerical approaches. Their radiative properties are calculated through the classical Mie theory using optical properties, n and k, and the diameter distribution function of pores. For Al_2O_3 plasma-sprayed samples, radiative properties are calculated using an electromagnetic approach, adapted to ceramics of complex structure.

The preliminary step, consisting of comparing measurements and predictions for YPSZ emission spectra, to validate the comprehensive approach, proved very satisfactory. Good agreement between experimental and numerical curves is observed.

The part of the study dedicated to Al_2O_3 samples of complex microstructure allows deduction of the following conclusions: the adopted numerical approach can be valid for this type of material provided that optical indexes are perfectly known for corresponding temperature and wavelength ranges. The numerical approach pointed out the necessity of a precise knowledge of the microstructure parameters. Consequently, MEB or tomography will be techniques suitable to obtain relevant structure parameters. Modeling the radiative emission from Al_2O_3 samples also shows that in the wavelength range where the material is optically thick (i.e., $\lambda > 11$ μm), surface scattering becomes prevalent compared to volume scattering. Consequently, our current model that does not consider this fundamental phenomenon, widely underestimates the spectral emission factor for the mid-infrared. To improve our predictive model, it is planned to couple with our code, a surface scattering code to take into account the roughness of the surface.

For pertinent use of an emission factor, a knowledge of the surface temperature is not sufficient. In particular, if the thickness of the ceramic layer is of the same order

of magnitude as the transport length of the radiation, a significant thermal gradient has great impact on the emission factor. For the example presented in this study, this configuration is encountered for the spectral range below 4 μm. But for a mid-infrared wavelength higher than 9 μm for our study—the transport length is much smaller than 100 μm, a thickness corresponding to a temperature difference of a few kelvins, while the ceramic layer is 1 mm thick with a total temperature difference of about 25 K. In this spectral range, no influence of a non-uniform inside temperature on the emission factor should be expected, which is confirmed by our measured spectra.

Acknowledgments Acknowledgment is made to the CEA Le Ripault. Plasma-sprayed samples studied in this study were indeed elaborated and characterized by the CEA LR. Acknowledgment is also made to the CEMHTI Orleans. They measured the optical indexes of alumina and yttria-stabilized zirconia ceramics at high temperature.

References

1. R. Bush, J. Patten, J. Fairbanks, MCIC 75-27, in *Proceedings of 1974 Gas Turbine Materials in the Marine Environment Conference* Castine, Maine
2. D.J. Wortman, B.A. Nagaraj, E.C. Duderstadt, Mater. Sci. Eng. A **121**, 433 (1989)
3. S.M. Meier, D.K. Gupta, 92-GT-203, ASME (1992)
4. A. Maricocchi, A. Bartz, D. Wortman, J. Therm. Spray Technol. **6**, 2 (1997)
5. F.O. Soechting, J. Therm. Spray Technol. **8**, 4 (1999)
6. R.A. Miller, J. Therm. Spray Technol. **6**, 1 (1997)
7. X.Q. Cao, R. Vassen, D. Stoever, J. Eur. Ceram. Soc. **24**, 1 (2004)
8. J.T. DeMasi, K.D. Sceffler, S. Bose, J. Eng. Gas Turbines Power **112**, 521 (1990)
9. P. Sadooghi, JQSRT **93**, 461 (2005)
10. R. Siegel, J.R. Howell, *Thermal Radiative Heat Transfer*, 3rd edn. (Hemisphere, New York, 1992)
11. R. Lopes, L.M. Maura, A. Delmas, J.F. Sacadura, 7th AIAA/ASME, Albuquerque, 1998, No. 98-2934
12. R.M. Sova, M.J. Linevsky, M.E. Thomas, F.F. Mark, Infrared Phys. Technol. **39**, 251 (1998)
13. J.F. Brun, *Thèse de doctorat de physique d'Orléans* (Université d'Orléans, Orleans, 2003)
14. D. Demange, M. Bejet, B. Dufour, QIRT 8th Conference, 2006
15. P. Sadooghi, JQSRT **92**, 403 (2005)
16. D. Ng, G. Fralick, Rev. Sci. Instrum. **72**, 2 (2001)
17. L. Robin, A. Delmas, T. Lanternier, QIRT **2**, 4 (2007)
18. L. Robin, A. Delmas, T. Lanternier, F. Oeldhoffen, V. Ducamp, IHTC 13, 2006
19. B. Rousseau, J.F. Brun, D. DeSousa Meneses, P. Echegut, Int. J. Thermophys. **26**, 1277 (2005)
20. D.R. Clarke, Surf. Coat. Technol. **163–164**, 67 (2003)
21. R. McPherson, Thin Solid Films **112**, 89 (1984)
22. J. Ilavsky, C. Berndt, J. Karthikeyan, J. Mater. Sci. **32**, 15 (1997)
23. J. Ilavsky, G. Long, A. Allen, C. Berndt, Mater. Sci. Eng. **A 272**, 215 (1999)
24. J.P. Heliot, *3rd International Workshop on Chiral Bi-isotropic and Bi-anisotropic Media* (Périgueux, France, 1994)
25. F. Cabannes, D. Billard, Int. J. Thermophys. **8**, 1 (1987)